Journal of Directed Energy, **1**, Spring 2004, 143–159

Stimulated Raman Scattering of Intense Free-Electron Laser Radiation in the Atmosphere

J. R. Peñano,* P. Sprangle, P. Serafim,† B. Hafizi,‡ and A. Ting

Plasma Physics Division, Naval Research Laboratory, Washington, D.C. 20375

Stimulated rotational Raman scattering is known to be one of the main factors limiting the propagation of high-power laser beams in the atmosphere. A set of three-dimensional, fully time-dependent propagation equations describing the stimulated Raman interaction and propagation of short, ~picosecond laser pulses and pulse trains is presented and discussed. The laser pulses considered in this study are indicative of those generated by a megawatt-class free-electron laser (FEL) based on a radio frequency linac. In addition to the Raman interaction, the equations include other effects such as the optical Kerr nonlinearity due to bound electrons and group velocity dispersion, both of which are important for FEL pulses. The effective time-dependent nonlinear refractive index containing both Kerr and Raman processes is derived. Numerical simulations based on solving the propagation equations in three dimensions show the detailed evolution of the Raman scattering instability for various pulse formats. Stabilization of the Raman instability for pulses with durations much shorter than the rotational period is demonstrated. The interaction of FEL pulses in a train through the Raman polarization field is also illustrated.

KEYWORDS: Atmospheric propagation, Free-electron laser, Stimulated Raman scattering

Nomenclature

A	complex-valued amplitude of electric field
c	speed of light in free space
$\boldsymbol{E}$	electric field
e	base of natural logarithm
$\hat{\boldsymbol{e}}_x$	unit vector along x axis
$\hbar$	Planck's constant divided by 2π
I, I_0	laser intensity
i	$\sqrt{-1}$
k, k_0	wavenumber; carrier wavenumber
m	mass of an electron
n, n_0, n_2, n_K, n_R	total, linear, nonlinear, Kerr, and Raman refractive indices

Received January 30, 2003; revision received April 16, 2003.

*Corresponding author; e-mail: penano@ppdmail.nrl.navy.mil.

†Department of Electrical Engineering, Northeastern University, Boston, MA 02115.

‡Icarus Research, Inc., P.O. Box 30780, Bethesda, MD 20824-0780.

$\boldsymbol{P}$	polarization field
P_{NL}	self-focusing critical power for optical Kerr nonlinearity
Q	Raman oscillator function
q	charge on an electron
r, r_0	radial spatial coordinate, laser spot size
t	time variable
v, v_g	velocity, group velocity
x	x coordinate
y	y coordinate
Z_R	Rayleigh range
z	z coordinate
β_2	group velocity dispersion parameter
Γ	damping rate
λ	wavelength
ψ	phase
Ω	transition frequency
$\omega, \omega_0, \omega_R$	frequency, carrier frequency, rotational frequency
∇	gradient operator
$\nabla_\perp^2$	transverse Laplacian operator

1. Introduction

Recent advances in laser technology have generated tremendous opportunities for the development of unique directed energy applications. For example, free-electron lasers (FELs) have the potential for both high peak power and high average power generation, along with a flexible pulse format.[11] For directed energy weapon (DEW) applications, it is estimated that on the order of a megawatt of average power will be required. The pulse train of a megawatt-class FEL driven by a radio frequency (RF) linac will likely be characterized by individual pulses with durations of ~1 ps and peak powers in the gigawatt range, separated by ~1 ns. These short, high-intensity laser pulses can undergo unique interactions with the atmosphere in which both linear and nonlinear processes play a central role. As a result of the high intensities, thermal blooming, bound electron anharmonicity (optical Kerr effect), and stimulated rotational Raman scattering (SRRS) can affect laser beam propagation. Because of the short duration of these pulses, thermal blooming is not significant for a single pulse. Thermal blooming will, however, be an important macroscopic effect in the propagation of long pulse trains. This effect is discussed in an article by Sprangle et al. elsewhere in this issue.[19] This paper will focus on the effects of SRRS and other processes, such as group velocity dispersion (GVD), which can affect the propagation of individual pulses in a megawatt-class FEL pulse train. The interpulse interactions of a pulse train are also illustrated.

SRRS in air is a quantum mechanical process involving the excitation of the rotational states of the molecular constituents of air by the laser pulse. It can be characterized as an instability that scatters laser energy into multiple Stokes and anti-Stokes frequency bands,[4] which, because of the dispersive properties of air, can propagate at different velocities and at large angles with respect to the initial laser pulse, causing a severe distortion of the laser envelope.[20] Theoretically, SRRS can be understood as a three-level interaction[4,7] through the energy level diagrams shown in Fig. 1. The molecular scatterer is assumed to have two rotational eigenstates, 1 (the ground state) and 2, with corresponding energies W_1 and W_2, and an excited state, e.g., an electronic or translational state, with energy $W_3 \gg W_2 - W_1$.

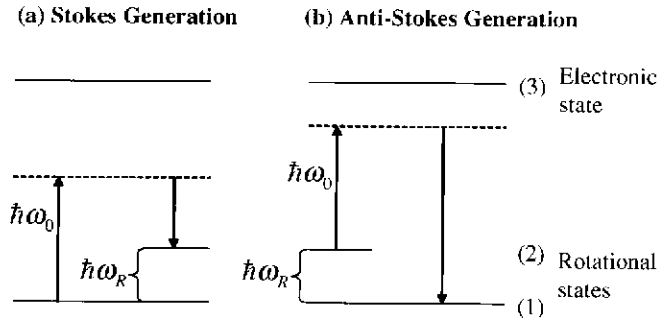

Fig. 1. Energy-level diagram of Stokes and anti-Stokes line generation from a three-level model of SRRS.

In this paper, we consider the nonresonant scattering process in which the central laser frequency $\omega_0 \neq \Omega_{31}, \Omega_{32}$, where $\Omega_{nm} = \Omega_n - \Omega_m$ and Ω_n is the frequency associated with state n. It is also assumed that $\Omega_{31}, \Omega_{32} \gg \omega_0 \gg \omega_R$, where $\omega_R \equiv \Omega_{21}$ is defined as the rotational frequency. In this situation, state 3 is not populated and the laser excites a virtual state that can decay to produce the Stokes and anti-Stokes radiation. The generation of Stokes radiation consists of a transition from state 1 to a virtual state, followed by a transition from the virtual state to state 2. In the process, a photon with frequency $\omega_- = \omega_0 - \omega_R$ is emitted. The generation of anti-Stokes radiation consists of a transition from state 2 to a virtual state followed by a transition from the virtual state to state 1, thereby emitting a photon at frequency $\omega_+ = \omega_0 + \omega_R$. Since the population of state 2 is much smaller than that of state 1 in thermal equilibrium, the anti-Stokes lines are generally much weaker than the Stokes lines.[4]

Stimulated Raman scattering of laser pulses propagating through air was studied extensively in the 1980s for longer (~nanosecond) laser pulses.[2,5,8,9,15] For altitudes below 100 km, the dominant Raman process for nanosecond pulses is due to scattering from N_2 molecules involving the S(8) rotational transition from the J = 8 to J = 6 rotational states, while the molecule remains in the vibrational ground state.[3] For a linearly polarized laser with wavelength 1 μm, experiments using nanosecond pulses indicate that the Raman gain coefficient is ~2.5 cm/TW (Ref. 5). The observed Raman shift for the S(8) rotational transition is 75 cm^{-1} ($\omega_R \sim 1.4 \times 10^{13}\ s^{-1}$), whereas the characteristic relaxation time for excited states is typically 0.1 ns at sea level.[8] A number of more recent experimental studies have employed ultrashort (~100-fs) laser pulses to investigate Raman scattering in air and various gasses.[12,14] In particular, the gain coefficient and damping rate have been measured and found to be different from those appropriate for longer pulses. The Raman scattering process for short pulses in air is expected to be markedly different from long-pulse scattering.[6,13] For example, the spectral width of a picosecond FEL pulse is comparable with the typical rotational frequency. Hence there is an appreciable signal at the Stokes frequency from the onset, and the number of e-foldings that the Stokes wave must undergo before it becomes comparable with the carrier signal amplitude is reduced relative to the number of e-foldings required for a longer, nanosecond pulse. GVD is also important for picosecond pulses propagating kilometer distances in air. The longitudinal spreading and frequency redistribution associated with GVD can affect the Raman process.

In a pulse train, interactions between pulses may also modify the Raman process. The leading pulses can excite molecular rotations that have a finite relaxation time. If the pulse

separation in time is not large compared with the relaxation time, subsequent pulses will encounter a perturbed medium, which could either enhance or suppress the Raman interaction of the trailing pulse.

One purpose of this paper is to present and discuss a model that takes into account these and other processes that are critical to the propagation of intense, short laser pulses in air. A closed system of equations is derived that describes the three-dimensional (3D), fully time-dependent propagation of a laser pulse in air along with the self-consistent evolution of the rotational Raman polarization field of the molecules. The propagation equation also includes the effects of GVD, bound electron anharmonicity (optical Kerr effect), and nonparaxial propagation. In some limits an analytical form for the effective nonlinear refractive index can be derived. For laser pulses short compared with the rotational period, this index is simply due to bound electron anharmonicity since the rotational levels cannot be excited. For longer laser pulses, the Kerr and Raman effects both contribute to the nonlinear index to the same order.[18]

In related articles by Sprangle et al.,[18,19] the effects of turbulence and ionization, among others, have been included in the formulation. For the purpose of this study, however, these other effects are neglected in order to isolate the Raman process.

A full-scale, 3D numerical simulation that solves the propagation equations presented in this paper has been developed at the Naval Research Laboratory (NRL). Because the simulation is fully time-dependent and self-consistent, it is capable of modeling the transient short-pulse Raman interaction and the consequent generation of broad multiwave spectra, as well as the more standard, long-pulse interaction. Simulations are used to model in detail the propagation of laser pulses of various formats undergoing SRRS. The dependence of the growth rate of the Raman instability on laser pulse length is investigated. The atmospheric propagation of pulse trains is also considered. In one example, a pulse train with characteristics similar to that of a megawatt-class FEL is modeled. Numerical results illustrate the interaction of pulses through the Raman polarization field.

This paper is organized as follows. Section 2 presents and discusses the set of nonlinear atmospheric propagation equations. The effective nonlinear index due to the Raman process is derived in Sec. 3. Section 4 presents the results of the numerical simulations. Conclusions are presented in Sec. 5.

2. Nonlinear Propagation Equation

An intense laser pulse propagating through the atmosphere is subject to a number of linear and nonlinear processes that include diffraction, GVD, and nonlinearities due to the polarization field associated with bound electrons and stimulated molecular Raman scattering. A general equation describing the atmospheric propagation of a laser pulse subject to these effects is outlined in this section. The details of the derivation will be published elsewhere. The starting point is the wave equation for the laser electric field $\boldsymbol{E}(x, y, z, t)$, given by

$$\left(\nabla_{\perp}^2 + \frac{\partial^2}{\partial z^2} - \frac{1}{c^2}\frac{\partial^2}{\partial t^2}\right)\boldsymbol{E} = \frac{4\pi}{c^2}\frac{\partial^2 \boldsymbol{P}}{\partial t^2}, \tag{1}$$

where $\nabla_{\perp}^2$ is the transverse Laplacian operator and z is the coordinate in the direction of propagation.

The polarization field is written as the sum of a linear and nonlinear contribution, $\boldsymbol{P} = \boldsymbol{P}_L + \boldsymbol{P}_{\mathrm{NL}}$. The laser electric field $\boldsymbol{E}(x, y, z, t)$, linear polarization field $\boldsymbol{P}_L(x, y, z, t)$,

and nonlinear polarization field $\boldsymbol{P}_{\mathrm{NL}}(x, y, z, t)$ are written in terms of complex amplitudes and a rapidly varying phase, i.e.,

$$\boldsymbol{E}(x, y, z, t) = A(x, y, z, t)\exp[i\psi(z, t)]\hat{\boldsymbol{e}}_x/2 + \text{c.c.}, \tag{2a}$$

$$\boldsymbol{P}_L(x, y, z, t) = P_L(x, y, z, t)\exp[i\psi(z, t)]\hat{\boldsymbol{e}}_x/2 + \text{c.c.}, \tag{2b}$$

$$\boldsymbol{P}_{\mathrm{NL}}(x, y, z, t) = P_{\mathrm{NL}}(x, y, z, t)\exp[i\psi(z, t)]\hat{\boldsymbol{e}}_x/2 + \text{c.c.}, \tag{2c}$$

where $\psi(z, t) = k_0 z - \omega_0 t$ is the phase, k_0 is the carrier wavenumber, ω_0 is the carrier frequency, $\hat{e}_x$ is a transverse unit vector in the direction of polarization, and c.c. denotes the complex conjugate. A propagation equation for the complex laser electric field amplitude, $A(x, y, z, t)$, is obtained by substituting Eqs. (2) into Eq. (1).

A closed system of equations is obtained by expressing the polarization field in terms of the laser electric field amplitude A. The linear polarization field modifies the refractive index while its derivatives with respect to frequency lead to temporal dispersion. The nonlinear polarization field is a consequence of bound electron anharmonicity (Kerr effect) and molecular rotation (stimulated Raman scattering effect). In terms of the linear susceptibility $\hat{\chi}_L(\omega)$, the linear polarization field is $\hat{P}_L(\omega) = \hat{\chi}_L(\omega)\hat{E}(\omega)$, where the overhat $\wedge$ denotes the temporal Fourier transform. The amplitude of the nonlinear polarization field can be written as a sum of P_K due to the optical Kerr effect of bound electrons and P_R due to stimulated Raman scattering from N_2 molecules. The nonlinear Kerr and Raman polarization fields are, respectively,

$$P_K(\boldsymbol{r}, t) = \frac{cn_K}{16\pi^2}|A(\boldsymbol{r}, t)|^2 A(\boldsymbol{r}, t), \tag{3a}$$

$$P_R(\boldsymbol{r}, t) = \chi_L Q(\boldsymbol{r}, t)A(\boldsymbol{r}, t), \tag{3b}$$

where n_K is the nonlinear index coefficient due to the Kerr effect, χ_L is the local susceptibility evaluated at the carrier frequency, and $Q(t)$ is the unitless Raman polarization function that satisfies Eqs. (5). Using Eqs. (1)–(3), the following propagation equation can be derived:

$$\left(\nabla_\perp^2 + 2ik_0\frac{\partial}{\partial z} - \frac{2}{v_g}\frac{\partial^2}{\partial z\partial\tau} - k_0\beta_2\frac{\partial^2}{\partial\tau^2}\right)A(x, y, z, \tau)$$

$$= -4\pi\frac{\omega_0^2}{c^2}\left[\frac{cn_K}{16\pi^2}|A|^2 + \chi_L Q(\tau)\right]A(x, y, z, \tau). \tag{4}$$

In Eq. (4), $k_0 = n_0(\omega_0)\omega_0/c$, $n_0(\omega) = \left[1 + 4\pi\hat{\chi}_L(\omega)\right]^{1/2}$ is the linear refractive index and β_2 is the GVD parameter. In writing Eq. (4) the independent variables (z, t) have been changed to the pulse frame variables (z, τ), where $\tau = t - z/v_g$, v_g is the linear group velocity of the laser pulse, and $\beta_g = v_g/c$. For air at one atmosphere and laser wavelengths of $\lambda \sim 1\ \mu$m, we note that $n_0^2 - 1 \sim 6 \times 10^{-4}(\chi_L \sim 5 \times 10^{-5})$ and $\beta_2 \sim 1.6 \times 10^{-31}\ \mathrm{s}^2/\mathrm{cm}$. Equation (4) describes the 3D propagation of a laser pulse in a dispersive nonlinear medium, characterized by the GVD parameter β_2, nonlinear refractive index n_K (Kerr effect), and stimulated Raman response function $Q(\tau)$.

Stimulated Raman scattering can arise through the interaction of the laser with the dipole moments of the molecular constituents of air (principally N_2 and O_2). The interaction may be analyzed quantum mechanically using a three-level model.[4,7,18] The result of this analysis is a pair of equations for the Raman response function $Q(\tau)$ and the population inversion

function $W(\tau)$ given by

$$\frac{\partial^2 Q}{\partial \tau^2} + \Omega_0^2 Q + 2\Gamma_2 \frac{\partial Q}{\partial \tau} = -\frac{\mu^2}{\hbar^2}\frac{\omega_R}{\Omega} W(\tau)|A(\boldsymbol{r}, \tau)|^2, \tag{5a}$$

$$\frac{\partial W}{\partial \tau} = \frac{\mu^2/\hbar^2}{\omega_R \Omega}\left(\frac{\partial Q}{\partial \tau} + \Gamma_2 Q\right)|A(\boldsymbol{r}, \tau)|^2 - \Gamma_1(1 + W), \tag{5b}$$

where $\Omega_0^2 = \omega_R^2 + \Gamma_2^2$, ω_R is the fundamental rotational frequency, μ is the effective dipole moment, Γ_1 and Γ_2 are phenomenological damping rates (Γ_1 is the population relaxation rate and Γ_2 is the dipole dephasing rate), and $\Omega \equiv \Omega_{32} \approx \Omega_{31}$ is the frequency associated with transition from a higher energy virtual state (state 3) to one of two lower energy rotational states (states 1 and 2).

3. Nonlinear Index Due to Raman and Kerr Effects

The Kerr and Raman nonlinearities contribute to the refractive index and can thus affect the propagation of the laser pulse. The Kerr nonlinearity is associated with self-phase modulation and nonlinear self-focusing, whereas the stimulated Raman process can lead to the generation of multiple Stokes and anti-Stokes waves that can propagate at large angles with respect to the propagation axis, thus scattering the laser energy.[20] In this section, the total nonlinear refractive index with both Kerr and Raman contributions is derived.

Retaining only the nonlinear propagation terms, Eq. (4) can be written as

$$2ik_0 \frac{\partial A}{\partial z} = -\left[n^2(z, \tau) - n_0^2\right]\frac{\omega_0^2}{c^2} A, \tag{6}$$

where n is the total refractive index in configuration space and n_0 is the linear index. The total time-dependent nonlinear index is identified as

$$\delta n(\tau) = n(\tau) - n_0 \approx n_K I(\tau) + 2\pi \chi_L Q(\tau), \tag{7}$$

which contains contributions from both the Kerr and Raman effects. In the limit $\Omega_R^2 \ll \Omega\Omega_0$, where $\Omega_R = \mu A_0/\hbar$ is the Rabi frequency associated with the peak electric field amplitude A_0, the population inversion associated with stimulated Raman scattering can be neglected, i.e., $W(\tau) \approx -1$, and the Raman response function, from solving Eq. (5a), is given by[10]

$$Q(z, \tau) = \frac{\mu^2}{\hbar^2}\frac{1}{\Omega}\int_0^\tau d\tau' e^{-\Gamma_2(\tau - \tau')} \sin[\omega_R(\tau - \tau')]|A(z, \tau')|^2. \tag{8}$$

The contribution of the Kerr effect to the polarization field is third order in the field amplitude. However, as seen from Eqs. (5)–(7), the Raman polarization field also has a contribution that is third order in the field amplitude and thus can contribute to the nonlinear refractive index at the same order as the Kerr effect. In the absence of Raman effects, the Kerr nonlinearity by itself can produce a modulational instability when the GVD parameter $\beta_2 < 0$ (Ref. 17).

As an example, consider a constant amplitude laser pulse with duration τ_L. The field amplitude can be written as $A = A_0[\Theta(\tau) - \Theta(\tau - \tau_L)]$, where $\tau = t - z/c$. From Eqs. (7) and (8), the nonlinear index within the pulse, i.e., $0 < \tau < \tau_L$, is $\delta n(\tau) = n_2(\tau) I(\tau)$, where the effective coefficient of nonlinearity is given by

$$n_2(\tau) = n_K + n_R\left\{1 - e^{-\Gamma_2 \tau}[\cos(\omega_R \tau) + (\Gamma_2/\omega_R)\sin(\omega_R \tau)]\right\}. \tag{9}$$

with

$$n_R = \frac{16\pi^2}{c}\frac{\mu^2}{\hbar^2}\frac{\chi_L}{\Omega}\frac{\omega_R}{\Omega_0^2}. \tag{10}$$

In the long-pulse limit ($\tau \gg 1/\Gamma_2$), the total nonlinear coefficient is given by $n_2 = n_K + n_R$, i.e., n_R represents the effective coefficient of nonlinearity due to Raman effects. For pulses short compared with the characteristic Raman times ($\tau \ll 1/\omega_R$, $\tau \ll 1/\Gamma_2$), the nonlinear refractive index is due to purely the bound electron response, i.e., $n_2 = n_K$.

The nonlinear coefficient due to Raman processes can also be written as

$$n_R = 2\frac{\omega_R}{\omega_0}\frac{\Gamma_2}{\Omega_0^2}cG, \tag{11}$$

where G is the Raman gain coefficient that characterizes the e-folding distance of the gain process for a long, constant amplitude laser beam, i.e., $A(z) \sim e^{GI_0 z}$. For a laser with wavelength 1 μm ($\omega_0 = 1.9 \times 10^{15}$ s^{-1}) and Raman parameters $\omega_R \sim 1.4 \times 10^{13}$ s^{-1}, $\Gamma_2 \sim 10^{10}$ s^{-1}, and $G \sim 2.5$ cm/TW (Ref. 5), the nonlinear coefficient due to the rotational Raman processes is $n_R = 5.6 \times 10^{-20}$ cm^2/W (Ref. 18). Assuming that bound electron and Raman effects are the dominant contributions to the nonlinear refractive index, the empirically determined value of $n_2 \approx n_K + n_R$ in the long-pulse regime is $\sim 5.6 \times 10^{-19}$ cm^2/W, giving $n_R/n_2 \approx 0.1$. More recent experiments, which propagate much shorter, $\sim$100-fs laser pulses with wavelength $\lambda = 0.8$ μm through air, suggest that the effective parameters for the short-pulse regime are $\omega_R \approx 1.6 \times 10^{13}$ s^{-1}, $n_R \approx n_K \approx 3 \times 10^{-19}$ cm^2/W, and $\Gamma_2 \approx 1.3 \times 10^{13}$ s^{-1} (Refs. 12 and 14), giving an effective gain coefficient of $G \approx 0.025$ cm/TW (Ref. 18).

4. Numerical Simulations

A numerical simulation based on solving Eq. (4) together with the stimulated Raman response given by Eqs. (5) has been developed at NRL. The simulation renders the laser pulse envelope on a Cartesian (x, y, τ) grid. The laser pulse is advanced in z according to Eq. (4) using a split-step spectral method[1] in which the linear terms are advanced in Fourier space and the nonlinear terms are handled in coordinate space. The equations describing the Raman response are solved at each z-step by a fourth-order Runge–Kutta integration. The following simulations will address the effects of pulse duration and pulse shape on Raman gain and the interpulse Raman interaction of a pulse train.

4.1. Effect of pulse duration on Raman gain

The first set of simulations shows the effects of pulse duration on Raman growth in the linear regime for single pulses. To isolate effects due to the Raman process, linear diffraction and the nonlinearity due to bound electrons (the Kerr nonlinearity) are neglected in these simulations. The paraxial approximation is also made so that the term in Eq. (4) containing the mixed derivative is neglected. GVD, which is important for short pulses, is retained.

The initial pulse envelope is taken to be Gaussian in the temporal coordinate, i.e., $A(z = 0, \tau) = A_0 \exp(-\tau/\tau_L)$ with no transverse variation (one dimensional; 1D). The laser wavelength $\lambda = 1$ μm. The parameters describing the Raman response are taken to be

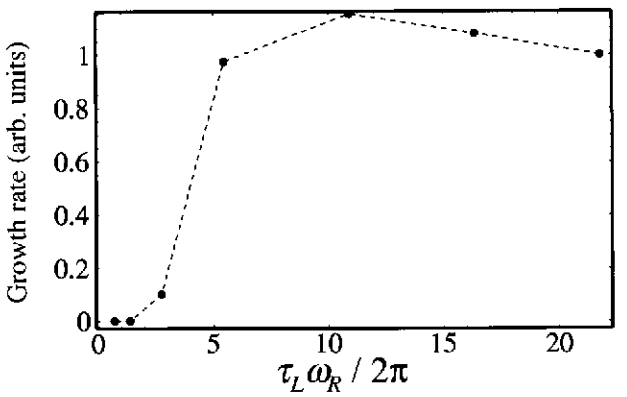

Fig. 2. Results of 1D simulations showing the dependence of the growth rate of the first Stokes line on pulse length for Gaussian pulses. Peak intensity is varied with pulse length to keep the fluence constant.

$\omega_R = 1.4 \times 10^{13}$ s^{-1}, $\Gamma_2 = 10^{10}$ s^{-1}, and gain coefficient $G = 2.5$ cm/TW. The GVD parameter $\beta_2 = 1.6 \times 10^{-31}$ s^2/cm.

In what follows, the pulse duration τ_L and peak intensity I_0 are varied keeping the product $\tau_L I_0 = 10^{-4}$ J/cm^2, which is proportional to the pulse energy, constant. For example, in these simulations, a 1-ps pulse would span $\omega_R \tau_L / 2\pi = 2.7$ rotational periods and have a peak intensity of 10^8 W/cm^2. For pulses that are long compared with the Raman period ($\omega_R \tau_L / 2\pi \approx 20$), the initial Fourier width of the laser spectrum is narrow compared with the rotational frequency. Hence there is a much smaller amplitude signal at the Stokes frequency initially for longer pulses compared with shorter pulses ($\omega_R \tau_L / 2\pi \approx 1$), which have a broader spectrum. In the long-pulse regime, the Stokes wave can undergo ~9 e-foldings before its amplitude is comparable with the amplitude of the main laser, as opposed to the short-pulse regime where only ~4 e-foldings are required. As the pulses propagate, exponential growth of multiple Stokes lines and lower amplitude anti-Stokes lines shifted from the central laser frequency by harmonics of ω_R are observed. To determine the Raman growth rate, the amplitude of the first Stokes line is measured as a function of propagation distance and fitted to an exponential function. Figure 2 summarizes the results of these simulations. The growth rate is seen to increase as the pulse length decreases from $\omega_R \tau_L / 2\pi > 20$ to $\omega_R \tau_L / 2\pi = 10$. For these longer pulses, transient effects are unimportant and the increase in the growth rate is due to the laser intensity, i.e., the source term for the Raman polarization field, increasing as the pulse length is made shorter. A dramatic reduction in the growth rate is observed when the pulse duration becomes comparable with or less than the rotational period. A number of factors lead to this reduction in the growth rate. First, these shorter pulses are in the transient interaction regime in which the pulse duration is shorter than the temporal growth rate of the Raman instability. Second, GVD for these short pulses tends to spread the pulse longitudinally and decrease the intensity, thereby decreasing the source term for the Raman polarization field.

4.2. 3D Simulations

When the transverse variation of the laser envelope is included, the stimulated Raman scattering process can be affected by a number of other 3D effects. For example, phase

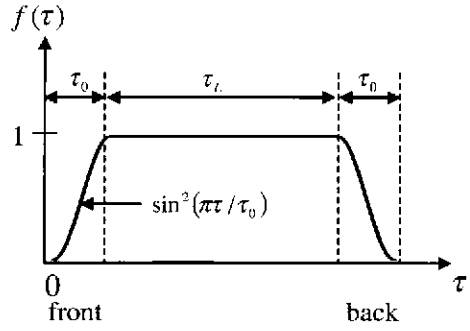

Fig. 3. Schematic diagram of the initial longitudinal laser envelope profile used in the simulations of Figs. 4–9.

matching conditions for the Stokes and anti-Stokes waves can cause them to propagate at large angles with respect to the laser propagation axis, thus scattering the laser energy. Also, nonlinear self-focusing can enhance the Raman process by increasing the laser intensity on axis. These effects will be illustrated in the following set of 3D simulations.

For the 3D simulations, the initial laser pulse envelope is given by $A(z = 0, r, \tau) = A_0 \exp(-r^2/r_0^2) f(\tau)$, where $r = \sqrt{(x^2 + y^2)}$ is the radial coordinate. The function $f(\tau)$, illustrated in Fig. 3, describes a longitudinal pulse profile with rise and decay times of τ_0 and a flat midsection of duration τ_L. The rise time $\tau_0 = \pi/2\omega_R \approx 0.1$ ps is chosen to optimally excite the Raman polarization field within the pulse. The transverse profile is a Gaussian with spot size r_0. For these simulations, all of the terms in Eq. (4) are retained. In the two examples presented in this section, we compare the propagation of pulses with durations of 1 and 10 ps. For both examples, the initial laser pulse has wavelength $\lambda = 1$ μm, spot size $r_0 = 15$ cm, and energy ~35 mJ. For the 10-ps example, this corresponds to a peak power of 3.5 GW and a peak intensity of 10^7 W/cm^2. For the 1-ps example, the peak power is 35 GW and the peak intensity is 10^8 W/cm^2.

The nonlinear refractive indicies associated with the bound electron anharmonicity and Raman process are taken to be equal, as indicated by previous short-pulse experiments,[12,14] i.e., $n_2 = n_R = 3 \times 10^{-19}$ cm^2/W. This corresponds to a nonlinear self-focusing power of $P_{NL} = \lambda^2/(2\pi n_0 n_2) \sim 5.9$ GW due to the bound electron nonlinearity.[16] Hence, the peak power for the 10-ps-pulse example is below the threshold for nonlinear self-focusing, whereas for the 1-ps-pulse example, it is above. Experimental determination of P_{NL} for short pulses is discussed by Ting et al. elsewhere in this issue.[21]

4.2.1. Long-pulse example. Figures 4 and 5 show, respectively, the contours of the intensity and Raman polarization function Q in the (t, x) plane $(y = 0)$ for the 10-ps $(\tau_L \omega_R/2\pi = 25)$ pulse at various propagation distances. The duration of the initial pulse $(z = 0)$ is long compared with the rotational Raman period, and the rise time is one quarter of the rotational period. This initial configuration is favorable for the Raman instability since the sharp rise time optimally excites the rotational Raman polarization and the long pulse duration contains many rotational periods. Figure 5a shows that the polarization function Q during the early phase of the instability is mainly localized near the axis of the laser pulse and rises in amplitude from the front of the pulse to the back. At $z = 20$ km, the laser intensity is strongly modulated at the rotational frequency. From the front to the middle of the pulse, the modulations increase in amplitude. Toward the back of the pulse, the on-axis

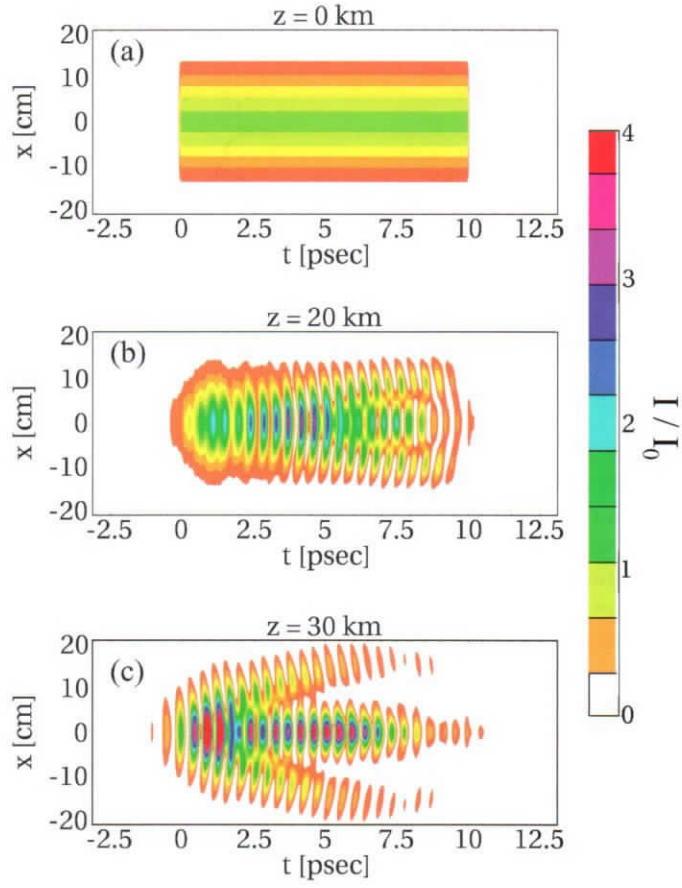

Fig. 4. Laser intensity contours in air as a function of time (t) and transverse position (x) at propagation distances $z =$ (a) 0, (b) 20, and (c) 30 km for a laser pulse with an initial Gaussian transverse profile ($r_0 = 15$ cm) and longitudinal profile indicated by Fig. 3 with $\lambda = 1$ μm, $\tau_0 = 0.1$ ps, $\tau_L = 10$ ps, and $I_0 = 10^7$ W/cm^2.

intensity decreases as laser energy begins to be scattered off-axis. As the pulse propagates, the modulations appear to move forward with respect to the original laser pulse. The Raman polarization field becomes broader in transverse extent (Fig. 5b) and continues to increase in amplitude as the instability develops. By $z = 30$ km, the intensity modulations, which were initially strongest at the back of the pulse, have grown in amplitude and have moved to the front of the pulse. The modulation, which is characterized by a longitudinal bunching of the laser energy, causes the peak intensity on-axis to become larger by a factor of 4 with respect to the initial intensity. Scattering of some of the laser energy off-axis is also evident, with the angle of scattering roughly five times larger than the vacuum diffraction angle. At $z = 30$ km, the Raman polarization field continues to broaden transversely, but it becomes highly peaked on-axis.

Figure 6 shows the evolution of the on-axis laser spectrum for the 10-ps pulse. The initial spectrum is narrow compared with the rotational period. The initial signal at the Stokes

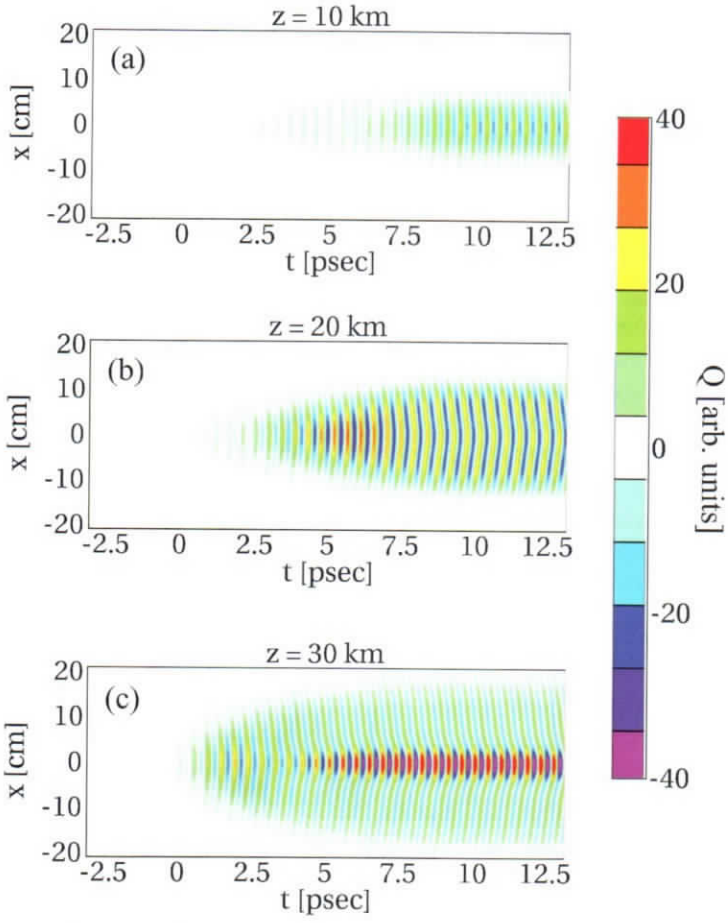

Fig. 5. Raman polarization function Q, associated with the laser pulse shown in Fig. 4, as a function of time and transverse position (x) at propagation distances z = (a) 10, (b) 20, and (c) 30 km.

frequency, $\Delta\omega = -\omega_R$, is two orders of magnitude smaller than the main pump signal at the laser frequency $\Delta\omega = 0$. At $z = 20$ km, the pump signal has decayed by a factor of 3, and the Stokes wave amplitude has grown to a comparable amplitude. The emergence of a much smaller amplitude, second-order Stokes line at $\Delta\omega = -2\omega_R$ and first-order anti-Stokes line at $\Delta\omega = \omega_R$ is observed. At $z = 30$ km, a broadening of the carrier, Stokes, and anti-Stokes lines is observed. The amplitude of the Stokes line is greater than that of the pump. It is evident that the intensity modulations shown in Fig. 4 are associated primarily with the lower frequency Stokes wave, which, because of the dispersive properties of air at ~ 1 μm, have a larger group velocity than the main laser pulse. Hence, the prominent growth of the Stokes wave is consistent with the observation that the laser intensity modulations travel forward with respect to the pulse.

4.2.2. Short-pulse examples. The first short-pulse example is for a $\sim$1-ps ($\tau_L \omega_R / 2\pi = 2.5$) laser pulse with the same spot size and energy as in the long-pulse example

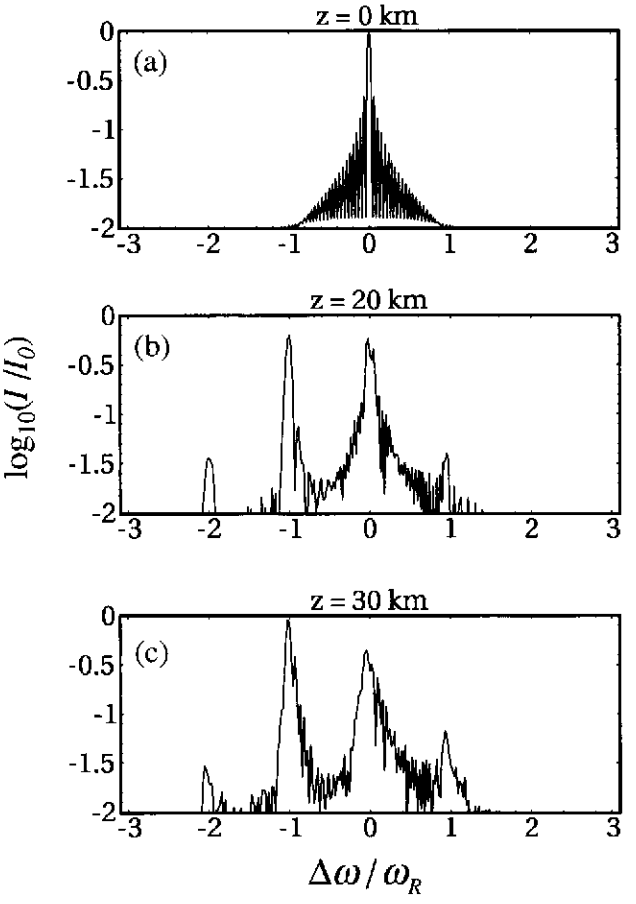

Fig. 6. Frequency spectrum (on-axis) of the laser pulse of Fig. 4 at z = (a) 0, (b) 20, and (c) 30 km showing prominent growth of first- and second-order Stokes lines.

discussed previously. Figure 7 shows the intensity contours for the short pulse in the (t, x) plane at $y = 0$ for propagation distances of $z = 0$, 0.4, 5, and 8 km. At $z = 0.4$ km, the pulse becomes modulated due to the longitudinal spreading out of the front and trailing portions of the pulse by GVD. The modulation frequency in this early stage of propagation is noticeably larger than the rotational frequency. A growing modulation at the rotational frequency becomes apparent at $z \sim 1$ km. At $z = 5$ km, the laser intensity is strongly modulated at the rotational frequency and has gained a factor of $\sim$2 in intensity on-axis. Similar to the long-pulse example, the modulations appear to travel faster than the main laser pulse. At $z = 8$ km, the modulations have surpassed the front edge of the main laser pulse, causing an apparent longitudinal spreading of the laser. No significant transverse spreading of the laser pulse is observed in this example.

The evolution of the on-axis frequency spectrum is shown in Fig. 8. Because of the shorter pulse duration, there is a much larger amplitude signal at the Stokes frequency initially compared with case of the longer pulse. Hence fewer e-foldings of the Stokes wave are required to saturate the Raman process and the pulse becomes highly distorted within a

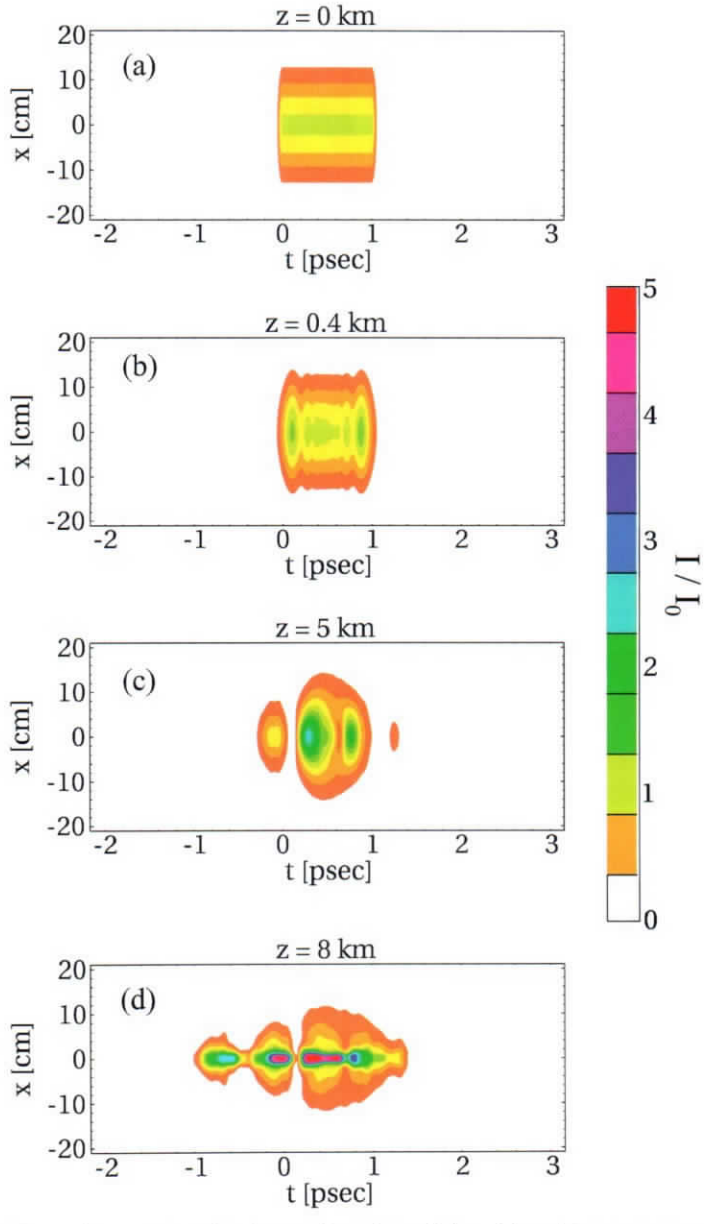

Fig. 7. Laser intensity contours in air as a function of time (t) and transverse position (x) at propagation distances $z =$ (a) 0, (b) 0.4, (c) 5, and (d) 8 km for a laser pulse with an initial Gaussian transverse profile ($r_0 = 15$ cm) and longitudinal profile indicated by Fig. 3 with $\lambda = 1$ μm, $\tau_0 = 0.1$ ps, $\tau_L = 1$ ps, and $I_0 = 10^8$ W/cm^2.

much shorter propagation distance relative to the long-pulse example. Similar to the long-pulse example, it is seen that the intensity modulations are due primarily to the growth of the Stokes wave, although in the case of the shorter pulse, the spectral width of the Stokes line is very broad.

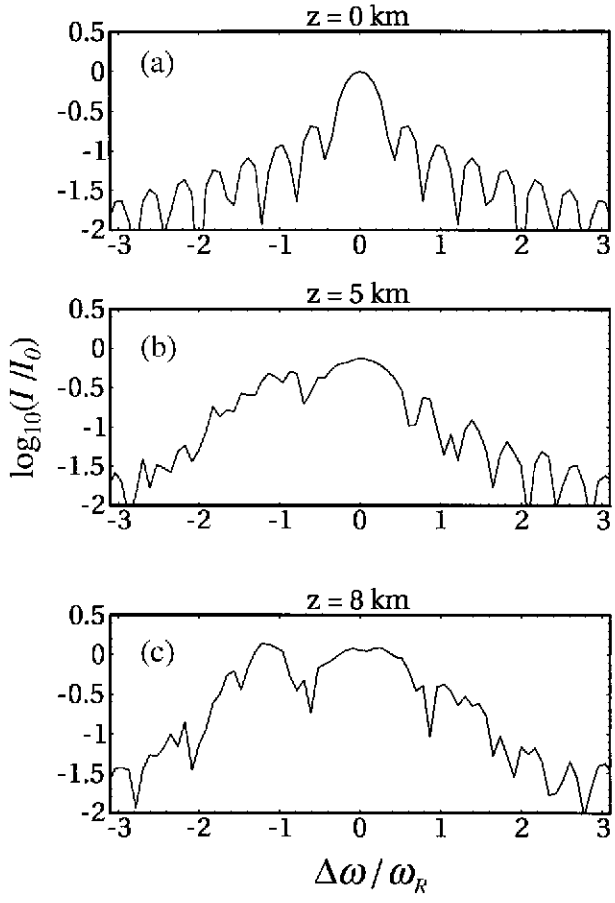

Fig. 8. Frequency spectrum (on-axis) of the laser pulse of Fig. 7 at z = (a) 0, (b) 5, and (c) 8 km.

Another simulation was performed with a shorter, 0.5-ps pulse, again keeping the spot size and pulse energy the same as in the previous two simulations. In this case, although the peak intensity was large (2×10^8 W/cm^2) and small amplitude modulations at the rotational frequency developed, these modulations did not grow appreciably as the pulse propagated. Propagation was dominated by GVD, which resulted in an almost symmetric longitudinal spreading of the entire pulse and a corresponding decrease in peak intensity. The pulse duration was observed to double after propagating ~0.5 km.

4.2.3. Raman scattering in pulse trains. The following simulations address the interpulse interactions of a pulse train. In a pulse train, the Raman polarization field excited by the leading pulses can affect the propagation of trailing pulses provided that the pulse separation is not much greater than the characteristic Raman relaxation time, which, in the absence of significant population inversion, is given by $1/\Gamma_2$. For pulse separations $<1/\Gamma_2$, the Raman polarization fields excited by a train of pulses can interfere constructively, thus amplifying the field and providing a greater seed for instability in trailing pulses. For the pulse train

of a megawatt-class FEL generated by an RF linac, the pulse separation is expected to be about 1 ns, which is 10 times the relaxation time. Hence, for this pulse configuration, interpulse interactions are expected to be negligible, although more detailed experimental measurements of the Raman relaxation time for ~picosecond pulses is required to verify this. For the purpose of this study, we consider separation times (~0.2 ns) comparable to the relaxation time to enhance pulse interaction effects.

Because of computational limitations, these simulations are carried out on a two-dimensional (2D), (τ, x) grid. The pulses are slablike, varying transversely in only one coordinate. In this situation the nonlinear focusing properties can differ significantly from fully 3D simulations when the propagation distances become comparable with the nonlinear focal length given by $Z_{\mathrm{NL}} = Z_R/\sqrt{(P_0/P_{\mathrm{NL}} - 1)}$ (Ref. 16), where $Z_R = n_0 \pi r_0^2/\lambda$ is the Rayleigh length and P_0 is the peak power. Hence, we consider examples where the pulse power $P_0 < P_{\mathrm{NL}}$ and the propagation distance $z < Z_R$. The simulation box is split up longitudinally into individual cells, each containing a single pulse in the train. Provided that no laser energy reaches the front or back cell boundaries, Eqs. (5) for the Raman response

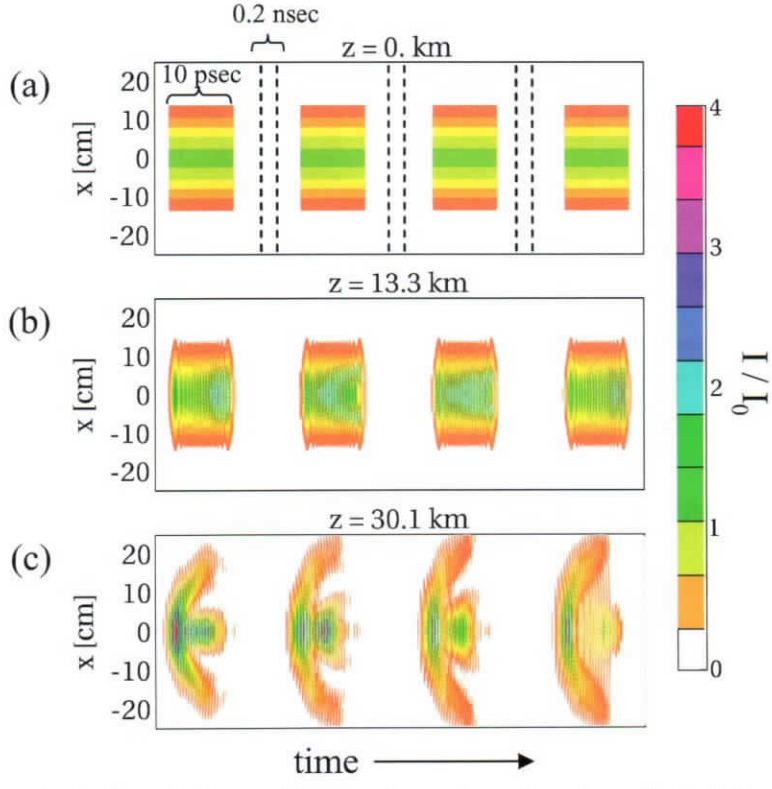

Fig. 9. 2D simulation of stimulated Raman interaction of a pulse train. Individual pulses at $z = 0$ have the same spot size, longitudinal profile, and peak intensity as the initial laser pulse shown in Fig. 4. Pulse separation is 0.2 ns, as shown in panel (a). Note the change in time scale between pulses. Panels (b) and (c) show intensity contours of the pulse train after propagating 13.3 and 30.1 km in air, respectively.

can be solved analytically at the cell interfaces to model the decay of the polarization field (both amplitude and phase) over arbitrary durations. The only information required for the analytic calculation is the amplitude and phase of the polarization field at the front of the cell boundary.

The first example is a train of pulses with properties initially identical to the pulse shown in Fig. 4a. The simulation box is shown schematically in Fig. 9a. Each pulse is 10 ps in duration. The vertical dashed lines denoting the cell boundaries represent breaks in the t-axis scale of 0.2 ns. The Raman damping time is taken to be $1/\Gamma_2 = 0.1$ ns. The Raman polarization field decays by a factor of ~8 across the cell boundaries. At a propagation distance of 13 km, there are noticeable differences in intensity modulations in each pulse. The second and third pulses of the train have developed slightly larger amplitude intensity modulations. At $z = 30$ km, obvious differences in transverse laser profiles become apparent.

5. Conclusions

SRRS of intense FEL radiation in the atmosphere has been investigated using a fully self-consistent, 3D numerical simulation. The key result from this study that is relevant to the atmospheric propagation of pulses generated by a megawatt-class FEL is that the Raman process can be a sensitive function of pulse format. Longer pulses with durations of >10 ps are more prone to scattering than short pulses (<1 ps). The scattering observed in the long-pulse example presented here tends to scatter laser energy off-axis, thus depleting the energy delivered to a remote target. Subpicosecond pulses are not as prone to scattering but are affected by GVD. However, GVD results in longitudinal redistribution with no transverse scattering of laser energy. Hence, for directed energy applications, it seems more beneficial to use a short-pulse format to suppress Raman scattering and deliver more energy on target. For the pulse train of a megawatt-class FEL, the interaction between pulses may not be important since the pulse separation (~1 ns) is much greater than the assumed Raman relaxation time of 0.1 ns. More definitive numerical studies, however, require detailed experimental measurements of the Raman parameters of air (rotation frequencies, relaxation times, nonlinear index) for picosecond pulses over a wide range of atmospheric conditions.

6. Acknowledgments

This work is sponsored by NAVSEA, the Joint Technology Office in support of the Navy DEW Program Office, and the Office of Naval Research.

References

[1]Agrawal, G.P., *Nonlinear Fiber Optics*, 2nd Ed., Academic Press, San Diego, CA (1995).

[2]Averbakh, V.S., A.I. Makarov, and V.I. Talanov, Sov. J. Quantum Electron. **8**, 472 (1978).

[3]Bloembergen, N., C.K.N. Patel, P. Avizonis, R.G. Clem, A. Hertzberg, T.H. Johnson, T. Marshall, R.B. Miller, W.E. Morrow, E.E. Salpeter, A.M. Sessler, J.D. Sullivan, J.C. Wyant, A. Yariv, R.N. Zare, A.J. Glass, and L.C. Hebel, Rev. Mod. Phys. **59**, S1 (1987).

[4]Boyd, R.W., *Nonlinear Optics*, Academic Press, San Diego, CA (1992).

[5]Henesian, M., C.D. Swift, and J.R. Murray, Opt. Lett. **10**, 565 (1985).

[6]Hickman, A.P., and W.K. Bischel, Phys. Rev. A **37**, 2516 (1988).

[7]Hickman, A.P., J.A. Paisner, and W.K. Bischel, Phys. Rev. A **33**, 1788 (1986).

[8]Kurnit, N.A., and D.E. Watkins, "Stimulated Rotational Raman Scattering in the Atmosphere," LAUR 87-0097, Los Alamos National Laboratory (1987).

[9]McDonald, G.S., G.H.C. New, L.L. Losev, A.P. Lutsenko, and M. Shaw, Opt. Lett. **19**, 1400 (1994).
[10]Mlejnek, M., M. Kolesik, J.V. Moloney, and E.M. Wright, Phys. Rev. Lett. **83**, 2938 (1999).
[11]Neil, G.R., C.L. Bohn, S.V. Benson, G. Biallas, D. Douglas, H.F. Dylla, R. Evans, J. Fugitt, A. Grippo, J. Gubeli, R. Hill, K. Jordan, G.A. Krafft, R. Li, L. Merminga, P. Piot, J. Preble, M. Shinn, T. Siggins, R. Walker, and B. Yunn, Phys. Rev. Lett. **84**, 662 (2000).
[12]Nibbering, E., G. Grillon, M. Franco, B. Prade, and A. Mysyrowicz, J. Opt. Soc. Am. B **14**, 650 (1997).
[13]Raymer, M.G., J. Mostowski, and J.L. Carlsten, Phys. Rev. A **19**, 2304 (1979).
[14]Ripoche, J.-F., G. Grillon, B. Prade, M. Franco, E. Nibbering, R. Lange, and A. Mysyrowicz, Opt. Commun. **135**, 310 (1997).
[15]Rokni, M., and A. Flusberg, IEEE J. Quant. Electron. **22**, 1102 (1986).
[16]Sprangle, P., E. Esarey, and J. Krall, Phys. Rev. E **54**, 4211 (1996).
[17]Sprangle, P., B. Hafizi, and J. Peñano, Phys. Rev. E **61**, 4381 (2000).
[18]Sprangle, P., J. Peñano, and B. Hafizi, Phys. Rev. E **66**, 046418 (2002).
[19]Sprangle, P., J.J. Peñano, A. Ting, B. Hafizi, and D.F. Gordon, J. Directed Energy **1**, 73 (2003).
[20]Syed, K.S., G.S. McDonald, and G.H.C. New, J. Opt. Soc. Am. B **17**, 1366 (2000).
[21]Ting, A., D. Gordon, D. Kaganovich, E. Briscoe, C. Manka, P. Sprangle, J. Peñano, B. Hafizi, and R. Hubbard, J. Directed Energy **1**, 131 (2004).

The Authors

Dr. Bahman Hafizi received B.Sc. and Ph.D. degrees in physics from Imperial College, London, in 1974 and 1978. He is president of ICARUS Research, Inc. He was previously a Research Associate in the Department of Astro-Geophysics at the University of Colorado and a Staff Scientist for SAIC. His research areas include propagation of ultraintense laser pulses, laser-driven electron accelerators, laser-plasma interactions, nonlinear optics, advanced sources of electromagnetic radiation with application to imaging, lithography, and remote sensing. He is an Associate of the Royal College of Science and a member of the American Physical Society, the European Physical Society, and IEEE.

Dr. Joseph R. Peñano received B.S. and Ph.D. degrees in plasma physics from the University of California, Los Angeles, in 1991 and 1998. He joined the NRL Beam Physics Branch in 2001. He conducts research on atmospheric propagation of ultrashort, high-intensity laser pulses for directed energy weapons and electronic countermeasure applications, advanced radiation sources, and laser-driven particle accelerators. He is the chief developer of HELCAP (High Energy Laser Code for Atmospheric Propagation). Prior to joining NRL, he was employed by LET Corp. and held a National Research Council postdoctoral fellowship. He received the NRL Alan Berman Publication Award in 2003.

Dr. Phillip Sprangle received his Ph.D. in applied physics from Cornell University in 1973. He is Chief Scientist and Head of the Beam Physics Branch at NRL. His research areas include atmospheric laser propagation, free-electron lasers, and laser acceleration physics. Dr. Sprangle is a fellow of the American Physical Society and the IEEE. He won the International Free Electron Laser Prize (1991), E.O. Hulburt Science and Engineering Award (1986), and Sigma Xi Pure Science Award (1994), as well as numerous publication awards. He has published more that 200 refereed scientific articles (28 letters) and holds 12 U.S. invention patents.

Dr. Antonio C. Ting received his Ph.D. degree in physics from the University of Maryland in 1984. He is a senior research physicist and the group leader of the High Field Physics Laboratory in the Plasma Physics Division of the Naval Research Laboratory. He conducts research on intense ultrashort pulse laser interactions with air, plasmas, and electron beams for directed energy weapons, standoff detections, electronic countermeasures, advanced x-ray sources, and particle accelerators. He is a Fellow of the American Physical Society and a member of Sigma Xi and the Directed Energy Professional Society.